

Supporting Information

Optimal rule-of-thumb design of NiFeMo layered double hydroxide nanoflakes for highly efficient and durable overall water-splitting at large currents

Akbar I. Inamdar*^a, Harish S. Chavan^a, Jun Ho Seok^b, Chi Ho Lee^b, Giho Shin^a, Sunjung Park^a,
Seungun Yeon^a, Sangeun Cho^a, Youngsin Park^c, Nabeen K. Shrestha^a, Sang Uck Lee*^b,
Hyungsang Kim*^a, Hyunsik Im*^a

^aDivision of Physics and Semiconductor Science, Dongguk University, Seoul 04620, South Korea

^bDepartment of Applied Chemistry, Center for Bionano Intelligence Education and Research, Hanyang University ERICA, Ansan 15588, South Korea

^cDepartment of Chemistry, College of Natural Science, Ulsan National Institute of Science and Technology (UNIST), Ulsan 44919, Korea

***Corresponding Authors**

*E-mail: akbarphysics2002@gmail.com (A. I. I.), hyunsik7@dongguk.edu (H. I.),
hskim@dongguk.edu (H. K.), sulee@hanyang.ac.kr (S. L.)

Table S1. NiFeMo electrocatalyst reported in the literature for the OER, HER and overall water splitting in alkaline electrolyte.

Sr. No	Catalyst	Synthesis method	Catalytic performance			High current density	Ref. (main text)
			OER (mV)	HER (mV)	Full Cell (V)		
1.	NiFeMo alloy inverse-opals	Solvent evaporation and electrodeposition followed by etching (multi-steps)	198	33	1.47	1.75 (V) @ 500 mAcm ⁻²	21
2.	Trimetallic NiFeMo	Hydrothermal followed by thermal annealing	238	45	1.45	-----	23
3.	Amorphous NiFeMo nanoparticles	Fast co-precipitation method	280	---	---	-----	24
4.	NiFeMo hybrid urea electrolysis	One-step electrodeposition	230	84.8	1.60	-----	28
5.	NiMoFe/Cu nanowire core-shell	Anodization of Cu-foam followed by electrodeposition of NiFeMO	520	45	1.82	-----	29
6.	NiFeMo Nanoparticles N-doped GO	solvothermal and annealing	330	-----	-----	-----	30
7.	NiFeMo oxyhydroxides	room-temperature sol-gel process	180	----	----	1.7 (V) @ 300 mAcm ⁻² 30% KOH	31
8.	Mo intercalated NiFe-LDH	hydrothermal	280	---	---	---	32
9.	Mo- Fe modified Ni(OH) ₂ /NiOOH Nanosheets	hydrothermal followed by electrochemical oxidation	300 @ 134.5 mAcm ⁻²	----	---	---	33

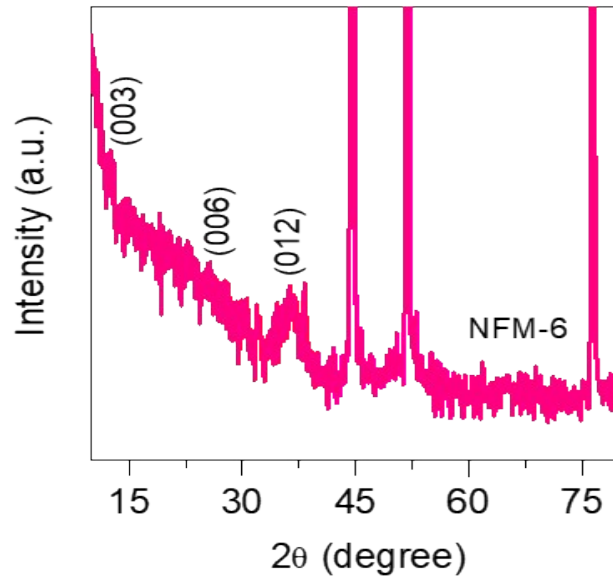


Figure S1. X-ray diffraction pattern of the NFM-6 ($\text{Ni}_{1.0}\text{Fe}_{1.75}\text{Mo}_{0.25}$ LDH), indicating low intensity peaks (0 0 3), (0 0 6) and (0 1 2) of NiFe-LDH.

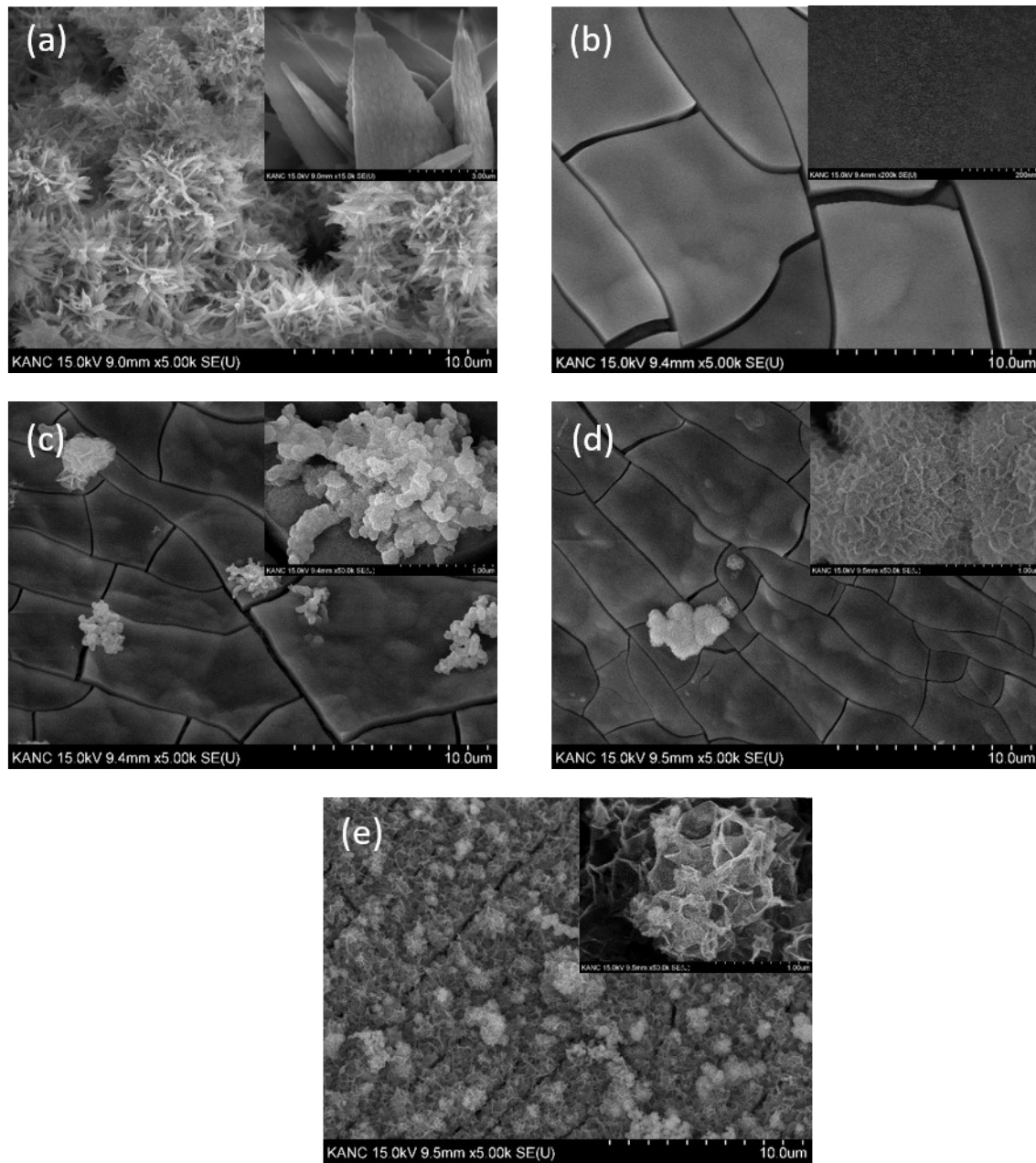


Figure S2. Scanning electron microscopy (SEM) images of as-grown (a) NFM-1 ($\text{Ni}_{1.0}\text{Fe}_{1.0}\text{Mo}_{1.0}$ LDH), (b) NFM-2 ($\text{Ni}_{1.0}\text{Fe}_{0.75}\text{Mo}_{1.25}$ LDH), (c) NFM-3 ($\text{Ni}_{1.0}\text{Fe}_{0.50}\text{Mo}_{1.50}$ LDH), (d) NFM-4 ($\text{Ni}_{1.0}\text{Fe}_{0.25}\text{Mo}_{1.75}$ LDH), and (e) NFM-5 ($\text{Ni}_{1.0}\text{Fe}_{1.50}\text{Mo}_{0.50}$ LDH). Inset displays an enlarged view. LDH, layered double hydroxide.

Table S2. Element concentration in the Ni_xFe_yMo_z LDH as detected by the inductively coupled plasma mass spectrometry (ICP-MS)

Sample	Ni (mg/ml)	Fe (mg/ml)	Mo (mg/ml)	Ni+Fe/Mo precursor	Ni+Fe/Mo actual
NFM-1	0.040771943	0.423984111	0.197090479	2.0	2.36
NFM-2	0.096585216	0.536277818	0.292419256	1.4	2.16
NFM-3	0.218887848	0.325636612	0.347816894	1.0	1.56
NFM-4	0.214864047	0.096298402	0.21379911	0.71	1.45
NFM-5	0.006060133	0.942296269	0.20067086	5.0	4.73
NFM-6	0.004587468	0.910036417	0.117996211	11.0	7.76

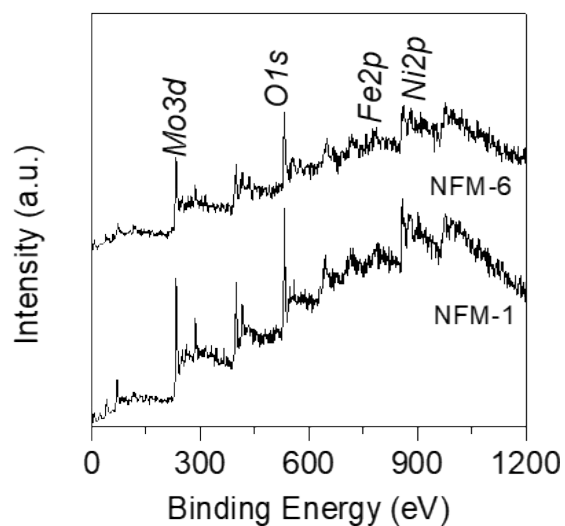


Figure S3. X-ray photoelectron spectroscopy (XPS) survey spectra for the NFM-1 and NFM-6 ($\text{Ni}_{1.0}\text{Fe}_{1.75}\text{Mo}_{0.25}$ LDH) catalysts revealing the presence of Ni, Fe, Mo, and O.

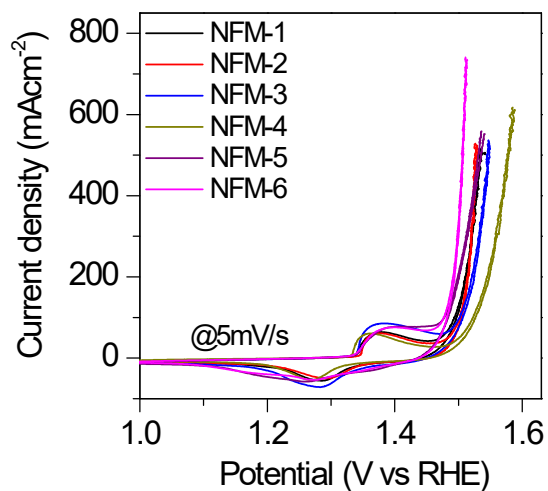


Figure S4. Cyclic voltammetry (CV) curves of all of the $\text{Ni}_x\text{Fe}_y\text{Mo}_z$ LDH catalysts recorded at a scan rate of 5 mVs^{-1} in a 1 M KOH electrolyte.

Table S3. Oxygen evolution reaction (OER) overpotential for the $\text{Ni}_x\text{Fe}_y\text{Mo}_z$ LDH electrocatalysts measured at 10 and 400 mA cm^{-2} .

Sample	Overpotential (mV)	
	@ 10 mAcm^{-2}	@ 400 mAcm^{-2}
$\text{Ni}_{1.0}\text{Fe}_{1.0}\text{Mo}_{1.0}$ LDH	246	330
$\text{Ni}_{1.0}\text{Fe}_{0.75}\text{Mo}_{1.25}$ LDH	229	295
$\text{Ni}_{1.0}\text{Fe}_{0.50}\text{Mo}_{1.50}$ LDH	249	338
$\text{Ni}_{1.0}\text{Fe}_{0.25}\text{Mo}_{1.75}$ LDH	240	332
$\text{Ni}_{1.0}\text{Fe}_{1.50}\text{Mo}_{0.50}$ LDH	209	265
$\text{Ni}_{1.0}\text{Fe}_{1.75}\text{Mo}_{0.25}$ LDH	200	255
NiFe LDH/NF	230	----

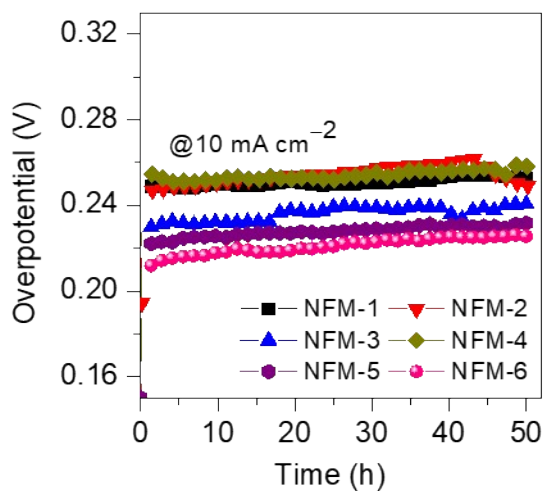


Figure S5. Chronopotentiometric stability curves over 50 h recorded at a constant current density of 10 mA cm^{-2} (without iR correction).

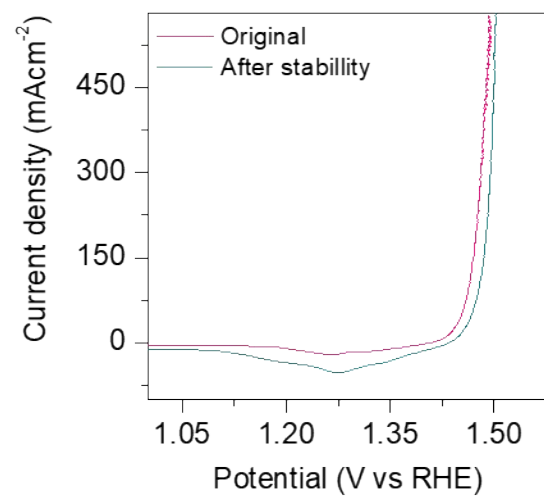


Figure S6. Overlap of the linear sweep voltammetry (LSV) curves (*iR*-corrected) of the NFM-6 electrocatalyst before and after stability testing for 50 hours in a 1 M KOH electrolyte.

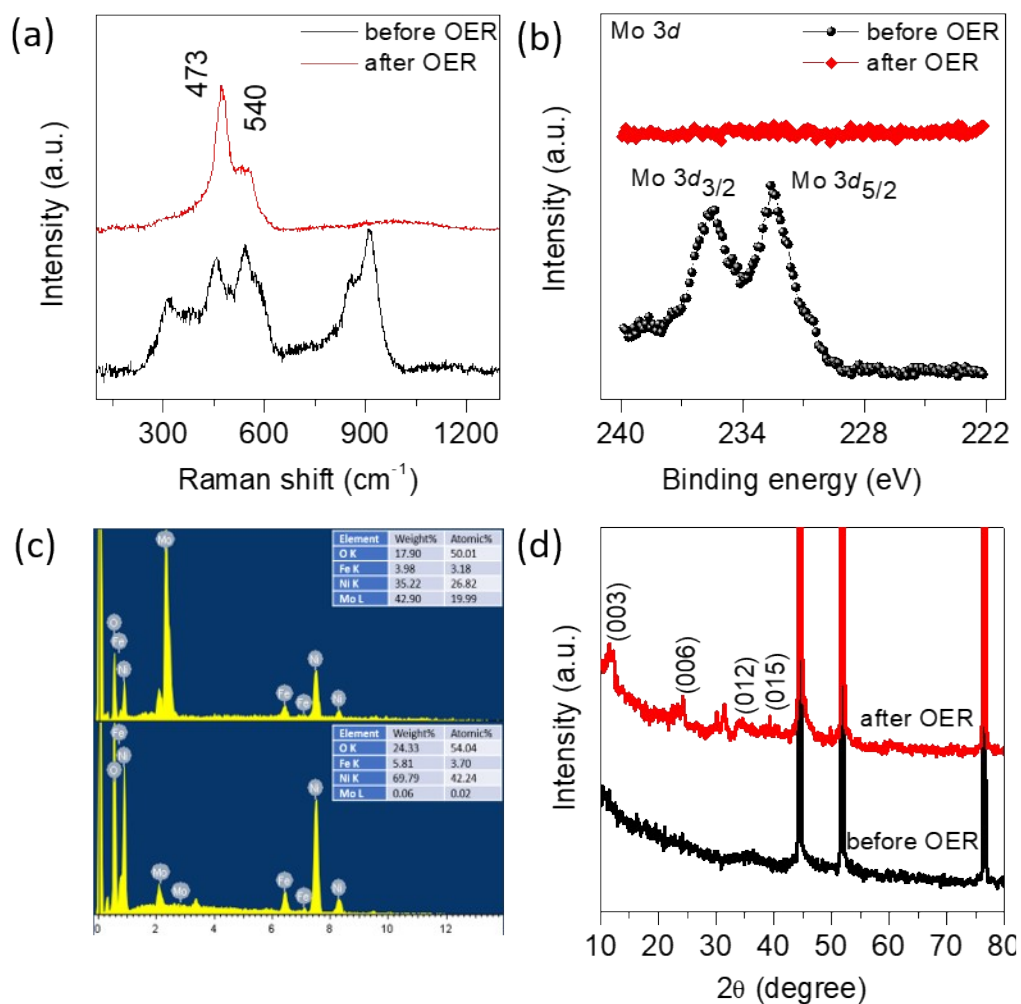


Figure S7. (a) Raman spectra, (b) Mo 3d XPS spectra, (c) and (d) EDAX spectra along with the elemental composition detected, and (d) X-ray diffraction patterns of the NFM-6 catalyst before and after stability testing at a current density of 10 mAcm⁻² for 50 hours in a 1 M KOH electrolyte.

The catalytic activity of the $\text{Ni}_x\text{Fe}_y\text{Mo}_z$ LDH samples was further analyzed using EIS and ECSA analysis; their Nyquist plots (**Figure S7**) were fitted using an equivalent circuit (the inset of **Figure S7a**) to determine their charge-transfer resistance (R_{ct}), solution resistance (R_s), and Warburg impedance (Z_w). The values for the EIS parameters obtained after OER testing are provided in **Table S2**. The NFM-6 sample exhibited the lowest charge-transfer resistance ($R_{ct} = 3.24 \Omega$), indicating rapid electron transfer at the electrode/electrolyte interface leading to stronger catalytic activity.

The ECSA, which is used to quantify catalytically active sites, was calculated by recording the CV in the non-faradaic region at scan rates of 50, 100, 200, 300, 400, and 500 mVs^{-1} in a 1M KOH electrolyte (**Figure S8**). It was determined for double-layer capacitance as follows: ¹

$$\text{ECSA} = C_{DL} / C_S \quad (1)$$

where C_S is the specific capacitance of a smooth planar surface (0.04 mF cm^{-2} for KOH), ², C_{DL} is the electrochemical double-layer capacitance, and A is the electrode area (1 cm^2 in this work). C_{DL} is determined from the slope of the current density (j) vs. scan rate (ν) (**Figure S9**). It can be observed in **Table S3** that the NFM-6 sample had the highest C_{DL} (0.117 mF cm^{-2} (ECSA = 2.925 cm^{-2}) compared with the other samples ($0.011\text{--}0.062 \text{ mF cm}^{-2}$). It is reasonable to assume that the ECSA obtained here reflects the real ECSA even after taking other factors such as ion intercalation, chemical capacitance, and the capacitance from the residual charge-transfer processes into consideration.

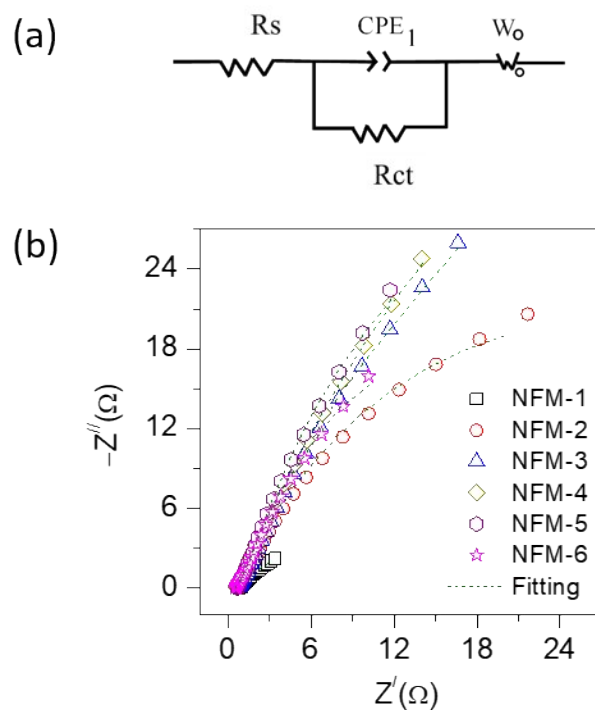


Figure S8. (a) Equivalent circuit diagram used to fit the EIS spectra, and (b) Nyquist plots recorded after OER testing at a frequency range of 1 Hz to 10 kHz in a 1 M KOH electrolyte.

Table S4. EIS parameters for the $\text{Ni}_x\text{Fe}_y\text{Mo}_z$ LDH electrocatalysts after OER testing.

Sample		R_s (Ω)	R_{ct} (Ω)
$\text{Ni}_{1.0}\text{Fe}_{1.0}\text{Mo}_{1.0}$	LDH	0.80	2.01
$\text{Ni}_{1.0}\text{Fe}_{0.75}\text{Mo}_{1.25}$	LDH	0.81	43.7
$\text{Ni}_{1.0}\text{Fe}_{0.50}\text{Mo}_{1.50}$	LDH	0.76	26.7
$\text{Ni}_{1.0}\text{Fe}_{0.25}\text{Mo}_{1.75}$	LDH	0.56	64.0
$\text{Ni}_{1.0}\text{Fe}_{1.50}\text{Mo}_{0.50}$	LDH	0.68	7.42
$\text{Ni}_{1.0}\text{Fe}_{1.75}\text{Mo}_{0.25}$	LDH	0.55	3.24

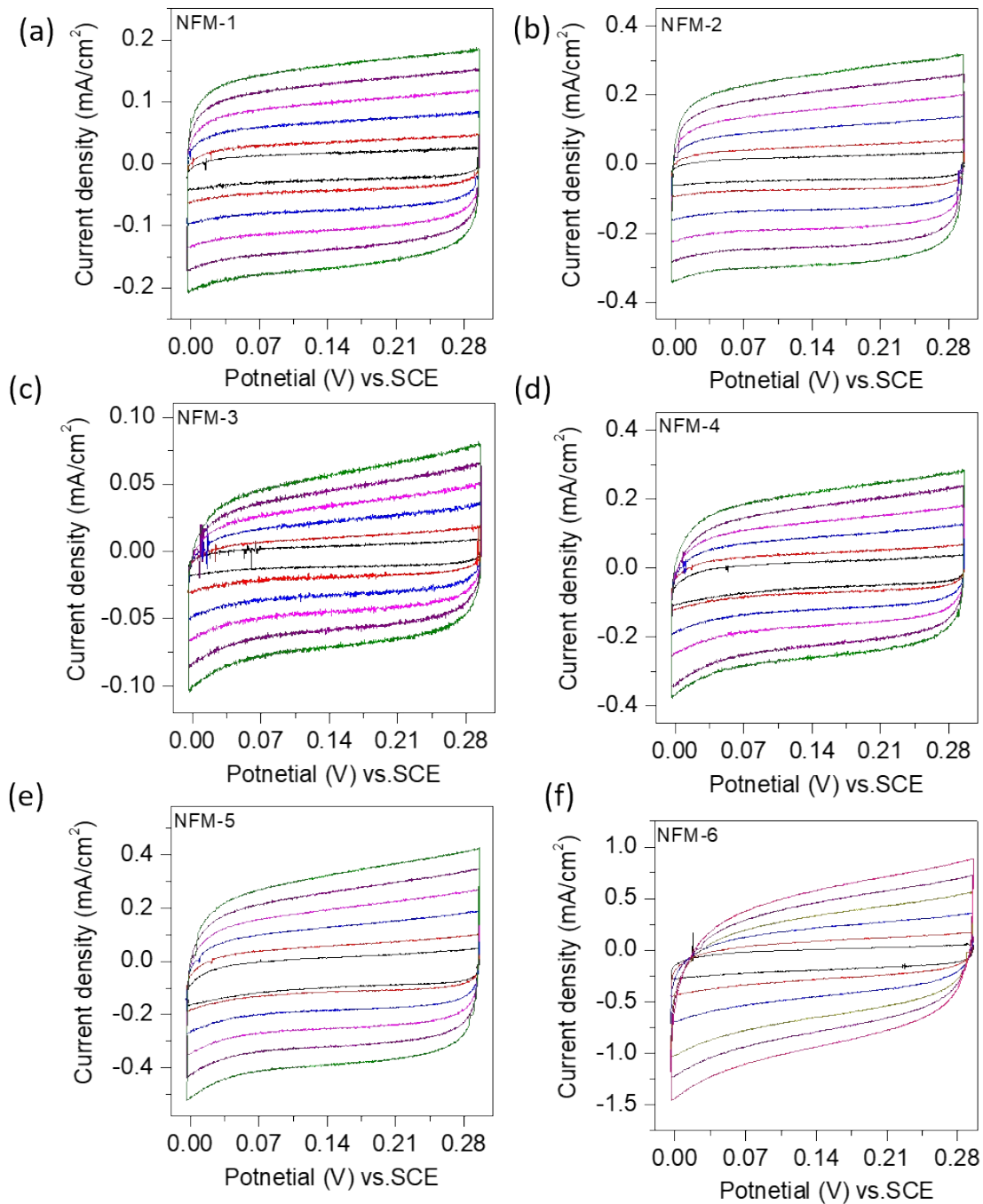


Figure S9. CV curves of for the $\text{Ni}_x\text{Fe}_y\text{Mo}_z$ LDH electrocatalysts recorded in the non-faradaic region at scan rates of 50, 100, 200, 300, 400, and 500 mVs^{-1} in a 1 M KOH electrolyte.

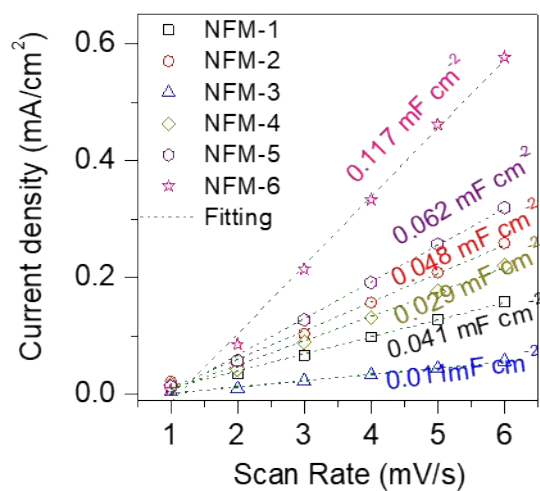


Figure S10. Non-faradaic current density (Δj) as a function of the scan rate ($\text{mV}\cdot\text{s}^{-1}$), with the slope corresponding to the double-layer capacitance (C_{DL}) of the $\text{Ni}_x\text{Fe}_y\text{Mo}_z$ LDH electrodes.

Table S5. ECSA parameters for the $\text{Ni}_x\text{Fe}_y\text{Mo}_z$ LDH electrocatalysts.

Sample	Double-layer capacitances (mF cm^{-2})	ECSA (cm^2)	Specific current density @ 230 mV (mA cm^{-2})
$\text{Ni}_{1.0}\text{Fe}_{1.0}\text{Mo}_{1.0}$ LDH	0.041	1.025	2.75
$\text{Ni}_{1.0}\text{Fe}_{0.75}\text{Mo}_{1.25}$ LDH	0.048	1.2	10.88
$\text{Ni}_{1.0}\text{Fe}_{0.50}\text{Mo}_{1.50}$ LDH	0.011	0.275	6.76
$\text{Ni}_{1.0}\text{Fe}_{0.25}\text{Mo}_{1.75}$ LDH	0.029	0.725	8.16
$\text{Ni}_{1.0}\text{Fe}_{1.50}\text{Mo}_{0.50}$ LDH	0.062	1.55	27.12
$\text{Ni}_{1.0}\text{Fe}_{1.75}\text{Mo}_{0.25}$ LDH	0.0117	2.925	28.63

To accurately evaluate the intrinsic catalytic activity for the OER, we normalized the LSV curves for the Ni_xFe_yMo_z LDH catalysts using the ECSA. The ECSA-normalized LSV curves are shown in **Figure S10**, revealing that the NFM-6 had the highest OER intrinsic activity, which was in accordance with the results observed for the geometrical area-based LSVs. The specific current density at an overpotential of 230 mV for the OER was also obtained from the ECSA-normalized LSV curves (**Table S3**). NFM-6 exhibited the highest current density, suggesting that it had higher intrinsic catalytic activity.

To obtain further insight into the active sites, we estimated the diffusion coefficient for the catalysts using the Randles-Sevcik equation³

$$J_p = 2.69 \times 10^5 n^{3/2} A C_0 D^{1/2} \nu^{1/2} \quad (2)$$

where C_0 represents the concentration of the electrolyte solution (mol cm⁻³), ν is the scan rate (V s⁻¹), D is the diffusion coefficient (cm² s⁻¹), J_p is the peak current, n is the number of electrons that take part in the redox reaction (assumed to be 1), and A is the electrode area (cm²). The CV curves recorded at a scan rate of 100 mVs⁻¹ in a 1 M KOH electrolyte (**Figure S11**) were used to calculate the diffusion coefficients (**Table S4** in the Supporting Information). The NFM-6 sample exhibited a significantly higher diffusion coefficient (13.82×10^{-10} m² s⁻¹) than the others (3.63 – 5.08×10^{-10} m² s⁻¹). Based on these results, it is reasonable to conclude that the enhanced OER activity of NFM-6 arises from the collective effect of its low charge-transfer resistance, high ECSA, and rapid ion diffusion.

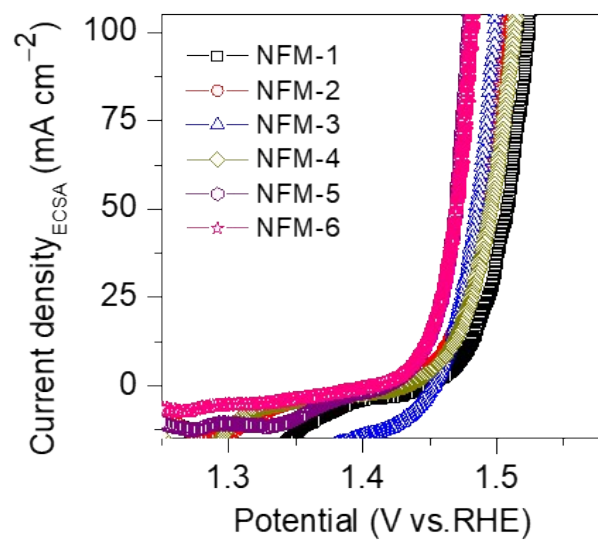


Figure S11. ECSA normalized LSV curves for the $\text{Ni}_x\text{Fe}_y\text{Mo}_z$ LDH electrocatalysts for OER

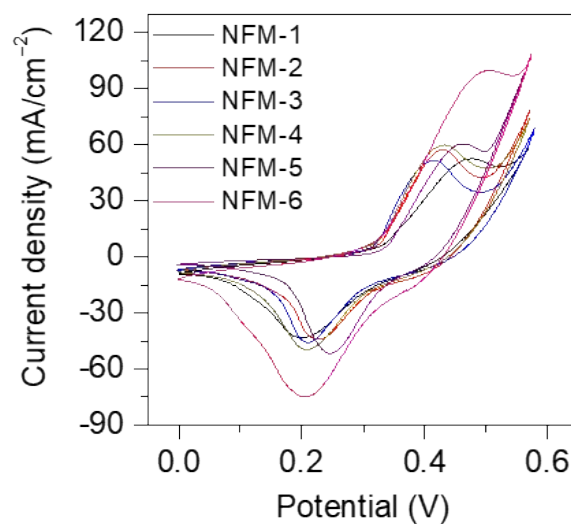


Figure S12. CV curves recorded at a scan rate of 100 mVs^{-1} in a 1 M KOH electrolyte used to determine the diffusion coefficient.

Table S6. Diffusion coefficient D of the $\text{Ni}_x\text{Fe}_y\text{Mo}_z$ LDH electrocatalysts estimated using the anodic peak current density.

Sample	Anodic peak Current density (mA cm^{-2})	Diffusion Coefficient ($\text{m}^2 \text{s}^{-1}$)
$\text{Ni}_{1.0}\text{Fe}_{1.0}\text{Mo}_{1.0}$ LDH	51.79	3.71×10^{-10}
$\text{Ni}_{1.0}\text{Fe}_{0.75}\text{Mo}_{1.25}$ LDH	57.20	4.53×10^{-10}
$\text{Ni}_{1.0}\text{Fe}_{0.50}\text{Mo}_{1.50}$ LDH	51.25	3.63×10^{-10}
$\text{Ni}_{1.0}\text{Fe}_{0.25}\text{Mo}_{1.75}$ LDH	59.60	4.92×10^{-10}
$\text{Ni}_{1.0}\text{Fe}_{1.50}\text{Mo}_{0.50}$ LDH	60.61	5.08×10^{-10}
$\text{Ni}_{1.0}\text{Fe}_{1.75}\text{Mo}_{0.25}$ LDH	99.90	13.82×10^{-10}

Table S7. HER overpotential of the $\text{Ni}_x\text{Fe}_y\text{Mo}_z$ LDH electrocatalysts measured at -10 mA cm^{-2} and -400 mA cm^{-2} .

Sample	Overpotential (mV) @ -10 mA cm^{-2}	Overpotential (mV) @ -400 mA cm^{-2}
$\text{Ni}_{1.0}\text{Fe}_{1.0}\text{Mo}_{1.0}$ LDH	86	252
$\text{Ni}_{1.0}\text{Fe}_{0.75}\text{Mo}_{1.25}$ LDH	149	339
$\text{Ni}_{1.0}\text{Fe}_{0.50}\text{Mo}_{1.50}$ LDH	155	331
$\text{Ni}_{1.0}\text{Fe}_{0.25}\text{Mo}_{1.75}$ LDH	136	322
$\text{Ni}_{1.0}\text{Fe}_{1.50}\text{Mo}_{0.50}$ LDH	161	336
$\text{Ni}_{1.0}\text{Fe}_{1.75}\text{Mo}_{0.25}$ LDH	185	359
NiFe LDH/NF	303	----

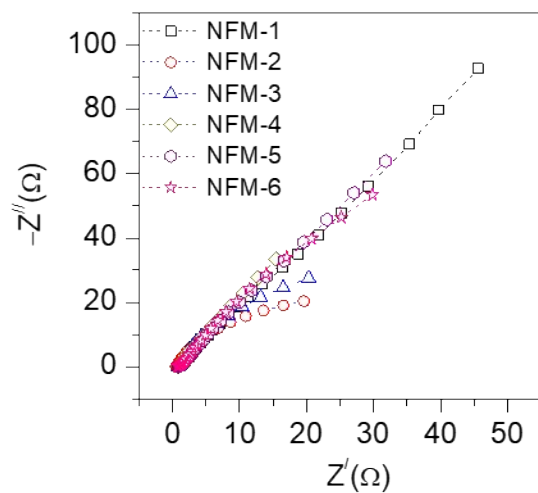


Figure S13. Nyquist plots recorded after HER testing at a frequency range of 1 Hz to 10 kHz in 1 M KOH electrolyte.

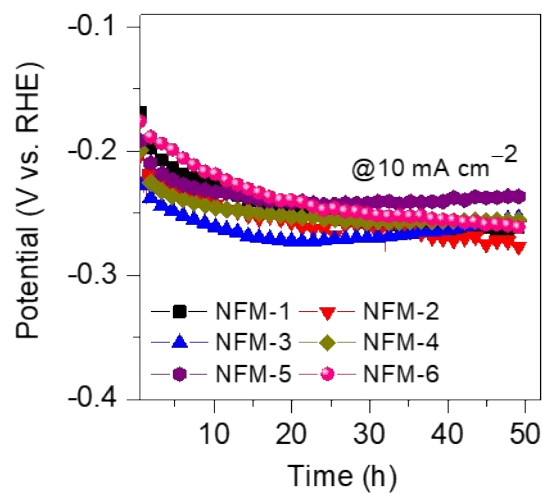


Figure S14. Chronopotentiometric stability curves over 50 h recorded at a constant current density of $-10 \text{ mA} \cdot \text{cm}^{-2}$ (without iR correction).

Table S8. Electrochemical impedance spectroscopy (EIS) parameters of the $\text{Ni}_x\text{Fe}_y\text{Mo}_z$ LDH electrocatalysts after HER testing.

Sample	R_s (Ω)	R_{ct} (Ω)
$\text{Ni}_{1.0}\text{Fe}_{1.0}\text{Mo}_{1.0}$ LDH	1.11	3.60
$\text{Ni}_{1.0}\text{Fe}_{0.75}\text{Mo}_{1.25}$ LDH	0.50	40.45
$\text{Ni}_{1.0}\text{Fe}_{0.50}\text{Mo}_{1.50}$ LDH	0.89	34.97
$\text{Ni}_{1.0}\text{Fe}_{0.25}\text{Mo}_{1.75}$ LDH	0.85	44.32
$\text{Ni}_{1.0}\text{Fe}_{1.50}\text{Mo}_{0.50}$ LDH	0.85	367.1
$\text{Ni}_{1.0}\text{Fe}_{1.75}\text{Mo}_{0.25}$ LDH	0.77	119

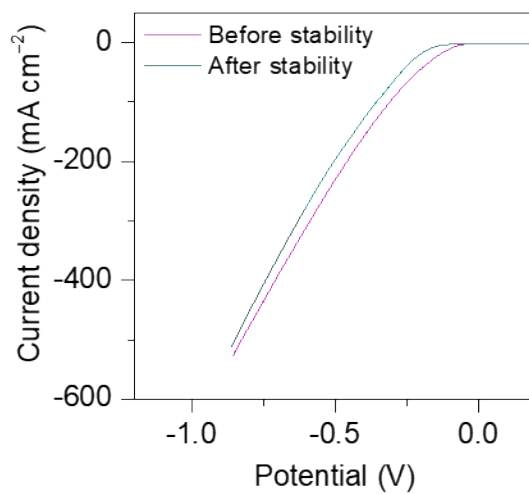


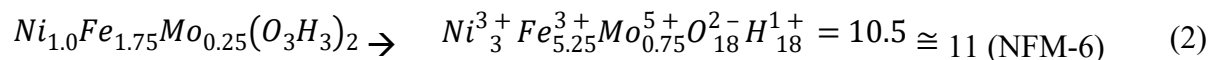
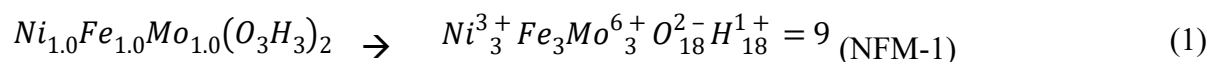
Figure S15. Polarization curves before and after HER stability testing. They remained unchanged, verifying the excellent stability of the NFM-1 catalyst.

Computational details and modeling

All *ab initio* calculations were performed with the Vienna *Ab initio* Simulation Package (VASP 5.4.4).⁴⁻⁷ We used the projector augmented wave (PAW) method^{8, 9} with generalized gradient approximation based on the Perdew-Burke-Ernzerhof (PBE)¹⁰ functional including the Hubbard *U* correction (GGA+*U*)¹¹. A plane-wave cutoff energy of 500 eV was used. Lattice constants and internal atomic positions were fully optimized until the residual forces were less than 0.04 eV/Å. The vacuum slab space of a unit cell in the z-direction was set to 15 Å to avoid interactions between layers. A 3x3 supercell was used as the substrate for all catalysts. The Brillouin zone was performed with a K-point grid of 3 x 3 x 1 based on the Monkhorst-Pack scheme^[12] using a k-point mesh with an interval of 0.05 Å⁻¹. For convenience in identifying the active site positions, and deprotonation order, we named them with Arabic numbers. Details regarding the naming of the active sites are also included in **Figure S15**.

Rational design of surface reconstructed NFM-1 and NFM-6 structures

We designed the NFM-1 and NFM-6 structures based on the valence states of the metals experimentally observed in XPS by removing an appropriate number of hydrogens from Ni_xFe_yMo_z LDH during the surface reconstruction process to form oxyhydroxides. The number of desorbed hydrogens was calculated using the following equations:



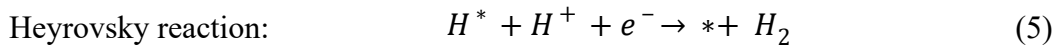
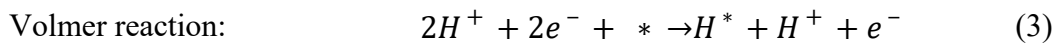
In addition, we systematically investigated the deprotonation process and confirmed that hydrogen desorption depends on the local environment induced by the surrounding transition metal. **Figure S15** shows that local structures with more Mo or Fe ions promote hydrogen desorption, whereas

local structures with more Ni ions inhibit deprotonation. The preference for single hydrogen desorption follows the order: $O_{\text{Mo}3} > O_{\text{Mo}2\text{Fe}} > O_{\text{NiFeMo}} > O_{\text{Ni}2\text{Mo}} > O_{\text{Fe}2\text{Ni}} > O_{\text{Fe}3} > O_{\text{Ni}3}$ for NFM-1 and $O_{\text{Fe}3} > O_{\text{Fe}2\text{Ni}} > O_{\text{Fe}2\text{Mo}} > O_{\text{NiFeMo}} > O_{\text{Ni}2\text{Fe}} > O_{\text{Ni}3}$ for NFM-6. Based on this, we constructed the most stable configurations of NFM-1 and NFM-6 within the $\text{Ni}_3\text{Fe}_3\text{Mo}_3(\text{OOH})_9$ and $\text{Ni}_3\text{Fe}_5\text{Mo}_1(\text{OO})_9\text{H}_7$ chemical formulas, respectively, as shown in **Figure S15-(b)**.

Gibbs free energy calculations for the HER and OER

Here, we employed the theoretically well-defined free energy diagram (FED) approach proposed by the Norskov group. It has been generally accepted for use in electrochemical studies based on density functional theory (DFT) calculations. To investigate catalytic reactions on specific surface structures, we generally employ the thermodynamic stability of the intermediates as the main descriptor, which determines the catalytic performance.^{13, 14}

The HER ($2\text{H}^+ + 2\text{e}^- \rightarrow \text{H}_2$) is a multi-step process that occurs on the catalyst surface, and there are two representative proposed mechanisms: Volmer-Tafel (V-T) and Volmer-Heyrovsky (V-H). Both mechanisms describe hydrogen atom adsorption and hydrogen molecule desorption using the following reactions:



where $*$ and H^* indicate an active site and adsorbed H atom on the catalyst surface, respectively. Because the equilibrium reduction potential for the HER is 0.0 V, the chemical potentials of the initial ($2\text{H}^+ + 2\text{e}^-$) and final states (H_2) should be the same. As such, with an ideal catalyst, its intermediate state should have the same chemical potential as the initial and final states under an

equilibrium potential, i.e., $U = 0.0$ V. However, actual catalytic observations deviate from this ideal behavior due to the binding strength of the intermediate on the surface of the catalyst. Therefore, the optimal binding free energy for hydrogen (H^*) should be zero for a spontaneous reaction without a barrier. Based on this theoretical approach, we calculated the reaction free energy of H^* on the $Ni_xFe_yMo_z$ LDH surface considering all possible active sites to identify the potential-determining step. HER activity can reasonably be represented by the V-T and V-H mechanisms using the following equation.

$$\Delta G_{H^*} = \Delta E_{H^*} + \Delta E_{ZPE} - T\Delta S_H \quad (6)$$

ΔE_{H^*} represents the hydrogen adsorption energy, which is calculated as follows:

$$\Delta E_{H^*} = E(\text{catalyst} + nH) - E(\text{catalyst} + (n-1)H) - 1/2E(H_2), \quad \text{where } E(\text{catalyst} + nH) \quad \text{and}$$

$E(\text{catalyst} + (n-1)H)$ represent the total energy of the $Ni_xFe_yMo_z$ LDH with n and $n-1$ adsorbed hydrogen atoms on the surface, respectively, while $E(H_2)$ represents the total energy of a gas phase

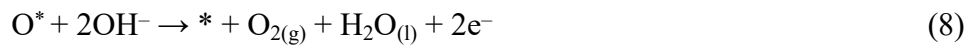
H_2 molecule. $\Delta E_{ZPE} = E_{ZPE}^{nH} - E_{ZPE}^{(n-1)H} - 1/2E_{ZPE}^{H_2}$, where E_{ZPE}^{nH} and $E_{ZPE}^{H_2}$ indicate the zero-point energy

of n chemisorbed hydrogens on the active site and the gas phase of H_2 , respectively. In addition,

$T\Delta S_H$ can be calculated from $-1/2S_{H_2}^0$ at 298K, where $S_{H_2}^0$ is the entropy of H_2 in the gas phase under

standard conditions and is obtained from the reference ($S_{H_2}^0 \cong 130$ J/mol*K).

For the OER, the four-electrons process with two reaction steps has generally been accepted; this process in an alkaline environment can be described as follows:



where * refers to the active site, and O* is adsorbed intermediate on the surface of the catalyst. The reaction Gibbs free energy of each electrochemical reaction step in the OER in an alkaline media can be expressed as follows:

$$\Delta G_1 = G_{O^*} + \mu_{H_2O(l)} + 2\mu_{e^-} - (G_* + 2\mu_{OH^-}) \quad (9)$$

$$\Delta G_2 = G_* + \mu_{O_2} + \mu_{H_2O(l)} + 2\mu_{e^-} - (G_{O^*} + 2\mu_{OH^-}) \quad (10)$$

These changes in the free energy can be calculated using the chemical potential of hydroxide, electrons, liquid water, and oxygen molecules (μ_{OH^-} , μ_{e^-} , $\mu_{H_2O(l)}$ and μ_{O_2}) and the free energy of each intermediate (G_{O^*} on the surface *).

From the calculated ΔG^{OER} values, we can determine the critical parameter for electrocatalytic activity, which is the size of the OER potential-determining step (G^{OER}) in the four-electron/two-step process. This is the specific reaction point with the largest ΔG in the OER elementary reaction steps, i.e., the concluding step to achieve a downhill reaction in the free energy diagram (FED) with increasing potential:

$$G^{OER} = \max [\Delta G_1, \Delta G_2]^0 \quad (11)$$

After calculating the largest ΔG , representing the bottleneck point for the OER, we can calculate the theoretical overpotential in an alkaline media using the following equation:

$$\eta^{OER} = (G^{OER}/2e) - xV, \quad x = 0.402 \text{ V} \quad (12)$$

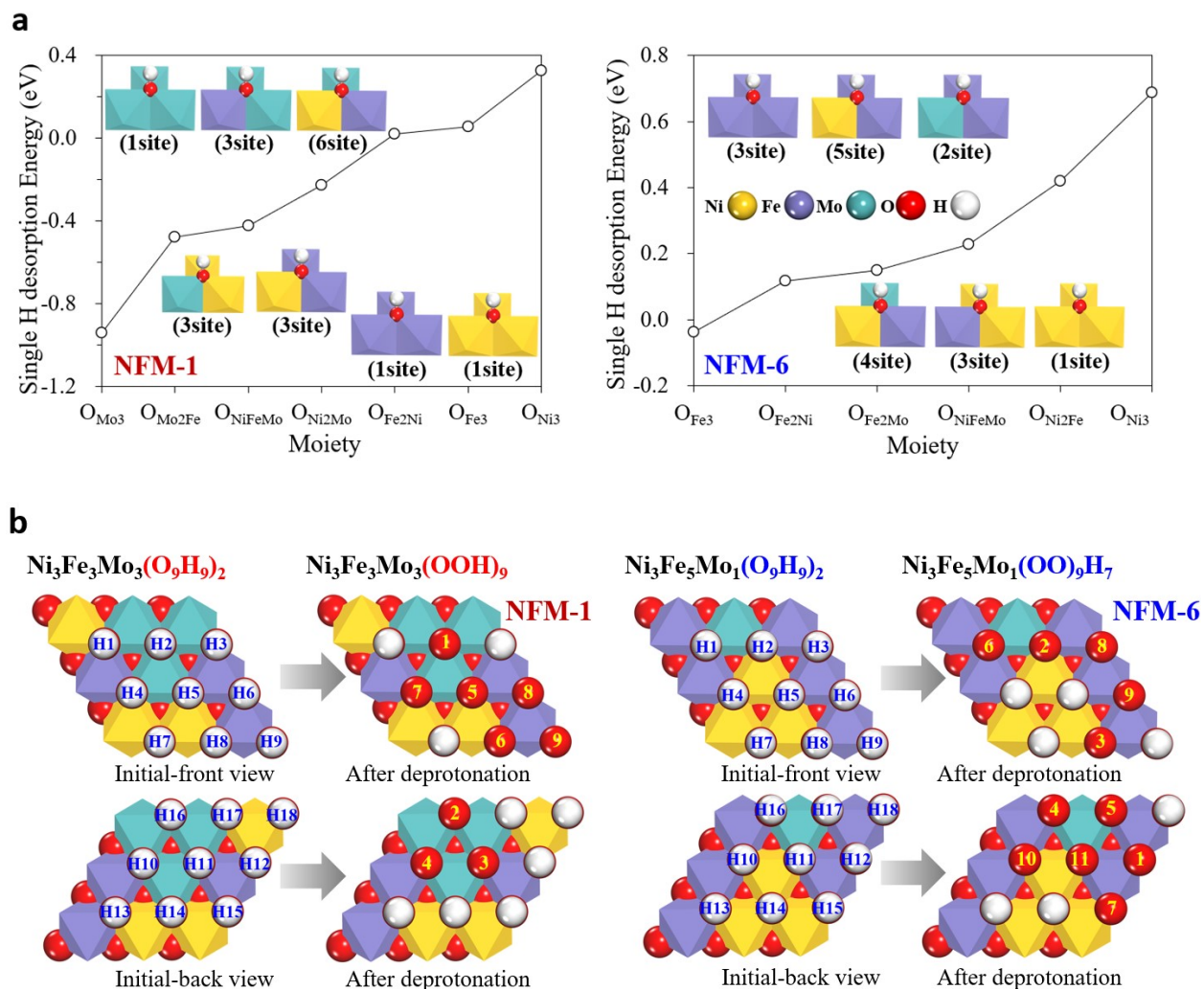


Figure S16. (a) Hydrogen desorption energy according to the local structure composed of different Ni, Fe and Mo metals. (b) Rational design of surface-reconstructed NFM-1 and NFM-6 structures. Yellow numbers indicate the order of deprotonation.

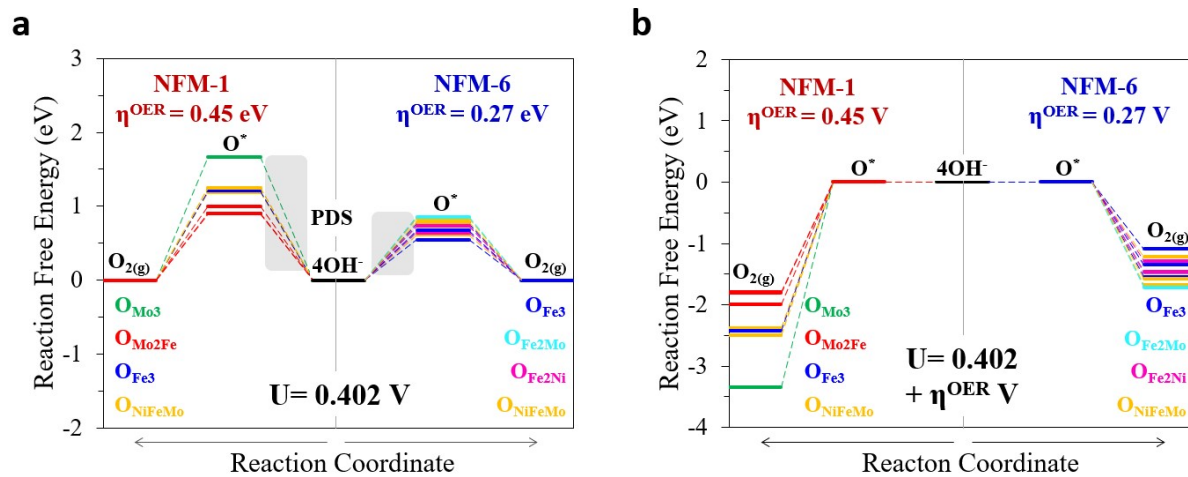


Figure S17. Free-energy diagrams of the OER according to the active sites of (a) NFM-1 and (b) NFM-6 at ideal potential ($U = 0.402$ V) and at overpotential ($U = 0.402 + \eta^{OER}$ V), in alkaline media.

Table S10. Calculated reaction free energies and over potential (η^{OER}) according to the active sites of NFM-1 and NFM-6.

Material	Index of active site	Type of active site	ΔG_1 (eV)	ΔG_2 (eV)	η^{OER} (V)
NFM-1	2	O _{Mo3}	2.48	-0.87	0.84
	4	O _{NiFeMo-1}	2.00	-0.39	0.60
	5	O _{NiFeMo-2}	2.00	-0.39	0.60
	6	O _{Fe3}	2.02	-0.41	0.61
	8	O _{NiFeMo-3}	2.05	-0.45	0.62
	9	O _{NiFeMo-4}	2.05	-0.45	0.62
	10	O _{Mo2Fe-1}	1.70	-0.09	0.45
	11	O _{Mo2Fe-1}	1.71	-0.10	0.45
	16	O _{Mo2Fe-3}	1.80	-0.19	0.50
NFM-6	1	O _{Fe2Mo-1}	1.65	-0.04	0.42
	2	O _{NiFeMo-1}	1.64	-0.03	0.42
	3	O _{Fe3-1}	1.35	0.26	0.27
	6	O _{Fe3-2}	1.57	0.03	0.39
	8	O _{NiFeMo-2}	1.41	0.19	0.30
	10	O _{Fe2Ni-1}	1.45	0.16	0.32
	11	O _{NiFeMo-3}	1.54	0.07	0.37
	12	O _{Fe3-3}	1.48	0.13	0.34
	15	O _{Fe2Ni-2}	1.53	0.08	0.36
	16	O _{Fe2Mo-2}	1.66	-0.05	0.43
17	O _{NiFeMo-4}	1.59	0.02	0.39	

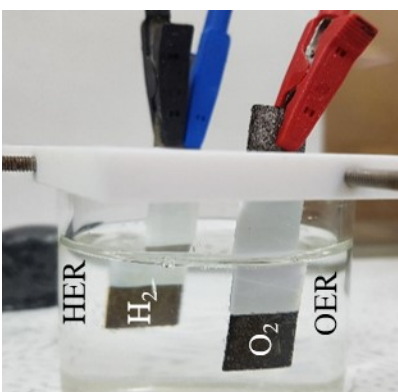


Figure S18. Overall water-splitting performance of the two-electrode water electrolyzer cell consisting of $\text{Ni}_x\text{Fe}_y\text{Mo}_z$ LDH electrodes.

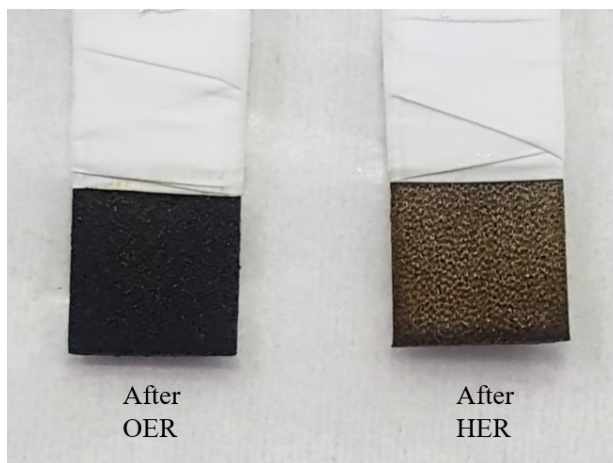


Figure S19. Photographic images of the NFM-6 electrocatalyst after full water-splitting testing. The electrode (at the anode side) turned black, which is probably due to surface oxidation of the catalyst, whereas the HER electrode (at the cathode side) remained unchanged.

Table S11. Performance comparison of various previously reported catalysts with the $\text{Ni}_x\text{Fe}_y\text{Mo}_z$ LDH electrocatalysts in this study.

Sr. No	Catalyst	Cell voltage (V), 1M KOH	Ref.
1.	$\text{Ni}_x\text{Fe}_y\text{Mo}_z$ LDH	1.59 @ 10 mA cm ⁻² 1.9 @ 500 mA cm ⁻² 2.1 @ 1000 mA cm ⁻²	This work
2.	Ce-doped NiFe-LDH	1.59	15
3.	CoFe@NiFe/NF	1.59	16
4.	NiCo ₂ S ₄ @NiFe LDH	1.6	17
5.	Ni-Mo/Cu	1.61	18
6.	Ni ₂ Fe ₁ Mo	1.62	19
7.	Ni ₂ P	1.63	20
8.	NiSe/NF	1.63	21
9.	CoFe LDH-F	1.63	22
10.	Ni/Mo ₂ C-NCNFs	1.64	23
11.	NiCo ₂ O ₄	1.65	24
12.	Ni/Mo ₂ C-PC	1.66	25
13.	NiCo-N/NiCo ₂ O ₄	1.68	26
14.	FeCoNi ternary alloy	1.687	27
15.	Co-NC@Mo ₂ C	1.69	28
16.	NiFe LDH/NF	1.70	29
17.	MoO _x /Ni ₃ S ₂ /NF	1.71	30

18.	Layered Co-Ni Hydroxide	1.75	31
19.	Ni ₃ FeN-NPs	1.81	32
20.	MoNi ₄ /MnO ₂ NiFe LDH/FeS	1.68 @ 100 mAcm ² 1.95 @ 300 mAcm ²	33
21	V-Ni ₃ S ₂ V-Ni ₃ S ₂ /NiFe LDH	1.77 @ 100 mAcm ²	34
22.	Single atom NiI Ir-C	1.62 @ 100 mAcm ²	35
23.	MoNi ₄ /MnO ₂ NiFeOOH(Se)	1.70 @ 100 mAcm ²	36
24.	Ni ₂ S ₃ /MnS-O Ni ₂ S ₃ /MnS-O	1.80 @ 100 mAcm ²	37
25.	Co@N-CS/N-HCP Co@N-CS/NHCP	1.85 @ 80 mAcm ²	38
26.	Ni@NiFe LDH Ni@NiFe LDH	1.78 @ 100 mAcm ²	39
27.	CoMoS _x CoMoS _x	1.89 @ 500 mAcm ²	40
28.	NiCo/NiCo-OH NiFe/NiFe-OH	1.74V @ 500 mA cm ⁻¹	41
29.	Co ₄ N-CeO ₂ Co ₄ N-CeO ₂	1.99 @ 500 mAcm ² 2.28 @ 1000 mAcm ²	42

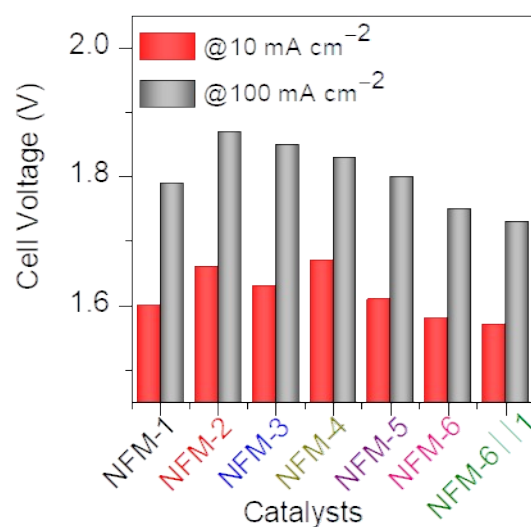


Figure S20. Bar diagram of the cell voltages required to reach current densities of 10 and 100 mA·cm⁻²,

Table S12. Performance comparison of the Ni_xFe_yMo_z LDH electrocatalysts.

Electrolyzer	Cell Voltage (V)	
	@ 10 mA cm ⁻²	@ 100 mA cm ⁻²
Ni _{1.0} Fe _{1.0} Mo _{1.0} LDH	1.60	1.79
Ni _{1.0} Fe _{0.75} Mo _{1.25} LDH	1.66	1.87
Ni _{1.0} Fe _{0.50} Mo _{1.50} LDH	1.63	1.85
Ni _{1.0} Fe _{0.25} Mo _{1.75} LDH	1.67	1.83

$\text{Ni}_{1.0}\text{Fe}_{1.50}\text{Mo}_{0.50}$ LDH	1.61	1.80
$\text{Ni}_{1.0}\text{Fe}_{1.75}\text{Mo}_{0.25}$ LDH	1.58	1.75
$\text{Ni}_{1.0}\text{Fe}_{1.75}\text{Mo}_{0.25}$ LDH	1.57	1.73
$\text{Ni}_{1.0}\text{Fe}_{1.0}\text{Mo}_{1.0}$ LDH		

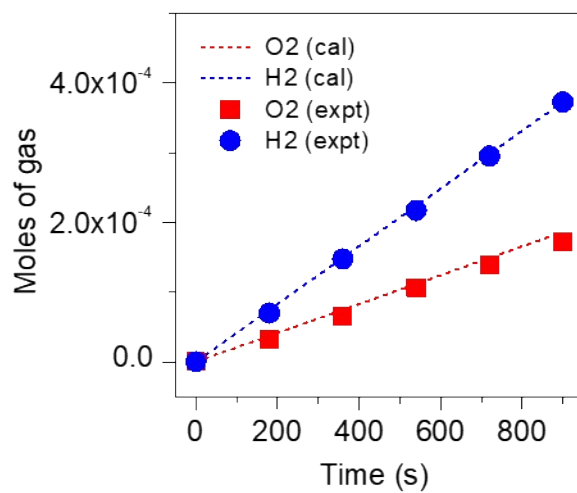
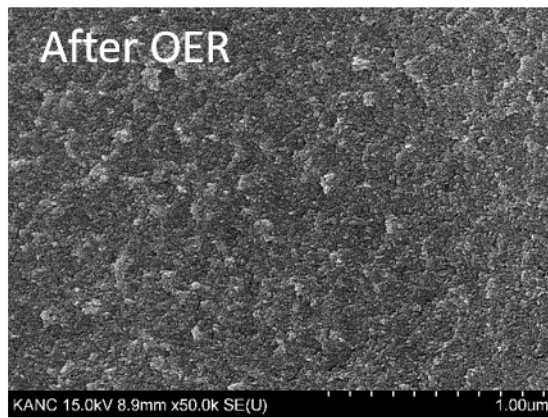


Figure S21. Faradic current efficiency for the O₂ and H₂ evolution of the NFM-6 || NFM-1 measured at 80 mAcm⁻² in a 1 M KOH aqueous electrolyte.

(a)



(b)

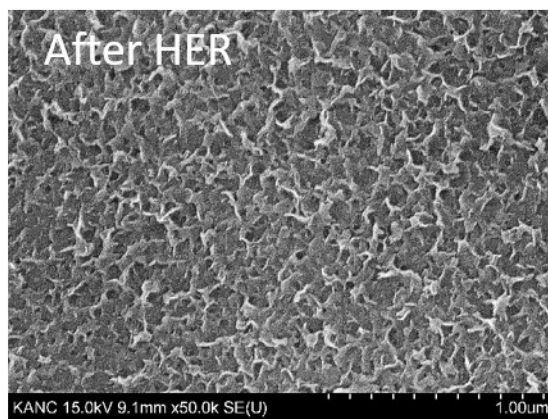


Figure S22. SEM images of the NFM-6 electrocatalyst after (a) OER and (b) HER stability testing.

References

1. N. Zhang, X. Feng, D. Rao, X. Deng, L. Cai, B. Qiu, R. Long, Y. Xiong, Y. Lu, Y. Chai, *Nat. Commun.* 2020, **11**, 4066.
2. C. C. L. McCrory, S. Jung, J. C. Peters, T. F. Jaramillo, *J. Am. Chem. Soc.* 2013, **135**, 16977.
3. C. Su, M. Qiu, Y. An, S. Sun, C. Zhao, W. Mai, *J. Mater. Chem. C* 2020, **8**, 3010.
4. G. Kresse, J. Hafner, *Physical Review B*, 1993, **48**, 13115-13118.
5. G. Kresse, J. Hafner, *Physical Review B*, 1994, **49**, 14251-14269.
6. G. Kresse, J. Furthmüller, *Computational materials science*, 1996, **6**, 15-50.
7. G. Kresse, J. Furthmüller, *Phys. Rev. B.*, 1996, **54**, 11169-11186.
8. P. Blichl, *Phys. Rev. B.*, 1994, **50**, 17953-17979.
9. G. Kresse, D. Joubert, *Phys. Rev. B.*, 1999, **59**, 1758.
10. J. P. Perdew, K. Burke, M. Ernzerhof, *Phys. Rev. Lett.* 1996, **77**, 3865.

11. S. Dudarev, G. Botton, S. Savrasov, C. Humphreys, *Phys. Rev. B.*, 1998, **57**, 1505.
12. H.J. Monkhorst, J.D. Pack, *Phys. Rev. B.*, 1976, **13**, 5188.
13. J. Rossmeisl, Z.-W. Qu, H. Zhu, G.-J. Kroes, J.K. Nørskov, *J. Electroanal. Chem.* 2007, **607**, 83-89.
14. J. K. Nørskov, J. Rossmeisl, A. Logadottir, L. Lindqvist, J.R. Kitchin, T. Bligaard, H. Jonsson, *J. Phys. Chem. B*, 2004, **108**, 17886-17892.
15. H. S. Jadhav, A. Roy, B. Z. Desalegan, J. G. Seo, *Sustain. Energy Fuels*, 2020, **4**, 312.
16. R. Yang, Y. Zhou, Y. Xing, D. Li, D. Jiang, M. Chen, W. Shi, S. Yuan, *Appl. Catal. B: Environ.* 2019, **253**, 131.
17. J. Liu, J. Wang, B. Zhang, Y. Ruan, L. Lv, X. Ji, K. Xu, L. Miao, J. Jiang, *ACS Appl. Mater. Interfaces* 2017, **9**, 15364.
18. S. Zhao, J. Huang, Y. Liu, J. Shen, H. Wang, X. Yang, Y. Zhu, C. Li, *J. Mater. Chem. A* 2017, **5**, 4207.
19. Y. Chen, C. Dong, J. Zhang, C. Zhang, Z. Zhang, *J. Mater. Chem. A* 2018, **6**, 8430.
20. L. A. Stern, L. Feng, F. Song, X. Hu, *Energy Environ. Sci.* 2015, **8**, 2347.
21. C. Tang, N. Cheng, Z. Pu, W. Xing, X. Sun, *Angew. Chem., Int. Ed.* 2015, **54**, 9351.
22. P. F. Liu, S. Yang, B. Zhang, H. G. Yang, *ACS Appl. Mater. Interfaces* 2016, **8**, 34474.
23. M. Li, Y. Zhu, H. Wang, C. Wang, N. Pinna, X. Lu, *Adv. Energy Mater* 2019, **9**, 1803185.
24. X. Gao, H. Zhang, Q. Li, X. Yu, Z. Hong, X. Zhang, C. Liang, Z. Lin, *Angew. Chem. Int. Ed.* 2016, **55**, 6290.
25. Z.-Y. Yu, Y. Duan, M.-R. Gao, C.-Ch. Lang, Y.-R. Zheng, S.-H. Yu, *Chem. Sci.* 2017, **8**, 968.

26. Z. Liu, H. Tan, D. Liu, X. Liu, J. Xin, J. Xie, M. Zhao, L. Song, L. Dai, H. Liu, *Adv. Sci.* 2019, **6**, 1801829.
27. Y. Yang, Z. Lin, S. Gao, J. Su, Z. Lun, G. Xia, J. Chen, R. Zhang, Q. Chen, *ACS Catal.* 2017, **7**, 469.
28. Q. Liang, H. Jin, Z. Wang, Y. Xiong, S. Yuan, X. Zeng, D. He, S. Mu, *Nano Energy* 2019, **57**, 746.
29. J. Luo, J.-H. Im, M. T. Mayer, M. Schreier, M. K. Nazeeruddin, N.-G. Park, *Science* 2014, **345**, 1593.
30. Y. Wu, G.-D. Li, Y. Liu, L. Yang, X. Lian, T. Asefa, X. Zou, *Adv. Funct. Mater.* 2016, **26**, 4839.
31. U. K. Sultana, J. D. Riches, A. P. O'Mullane, *Adv. Funct. Mater.* 2018, **28**, 1804361.
32. Q. Chen, R. Wang, M. Yu, Y. Zeng, F. Lu, X. Kuang, X. Lu, *Electrochimica Acta* 2017, **247**, 666.
33. S. Niu, W.-J. Jiang, T. Tang, L.-P. Yuan, H. Luo, J.-S. Hu, *Adv. Funct. Mater.* 2019, **29**, 1902180
34. J. Zhou, L. Yu, Q. Zhu, C. Huang, Y. Yu, *J. Mater. Chem. A*, 2019, **7**, 18118.
35. Y. Zhao, T. Ling, S. Chen, B. Jin, A. Vasileff, Y. Jiao, L. Song, J. Luo, S.-Z. Qiao, *Angew. Chem. Int. Ed. Engl.* 2019, **58**, 12252.
36. S. Niu, W.-J. Jiang, Z. Wei, T. Tang, J. Ma, J.-S. Hu, L.-J. Wan, *J. Am. Chem. Soc.* 2019, **141**, 7005.
37. Y. Zhang, J. Fu, H. Zhao, R. Jiang, F. Tian, R. Zhang, *Appl. Catal. B Environ.* 2019, **257**, 117899.

38. Z. Cai, X. Bu, P. Wang, W. Su, R. Wei, J. C. Ho, J. Yang, X. Wang, *J. Mater. Chem. A*, 2019, **7**, 21722.
39. Z. Chen, Y. Ha, H. Jia, X. Yan, M. Chen, M. Liu, R. Wu, *Adv. Energy Mater.* 2019, **9**, 1803918.
40. X. Shan, J. Liu, H. Mu, Y. Xiao, B. Mei, W. Liu, G. Lin, Z. Jiang, L. Wen, L. Jiang, *Angew. Chem. Int. Ed. Engl.* 2019, **59**, 1659.
41. Y. Luo, Z. Zhang, F. Yang, J. Li, Z. Liu, W. Ren, S. Zhang, B. Liu, *Energy Environ. Sci.*, 2021, **14**, 4610.
42. H. Sun, C. Tian, G. Fan, J. Qi, Z. Liu, Z. Yan, F. Cheng, J. Chen, C.-P. Li, M. Du, *Adv. Funct. Mater.* 2020, **30**, 1910596.